Available online at www.sciencedirect.com
ScienceDirect
Trans. Nonferrous Met. Soc. China 35(2025) 3677−3696
Transactions of Nonferrous Metals Society of China
www.tnmsc.cn

Effect of Y content on mechanical properties and electromagnetic interference shielding effectiveness of Mg−6Zn−*x*Y−1La−0.5Zr alloy

Wen-long XU [1,2], Xian-hua CHEN[1,2], Lu DENG[1,2], Guan-zheng ZHU[3], Yuan YUAN[1,2], Fu-sheng PAN[1,2]

1. College of Materials Science and Engineering, Chongqing University, Chongqing 400045, China;
2. National Engineering Research Center for Magnesium Alloys, Chongqing University, Chongqing 400045, China;
3. AECC Guiyang Engine Design Research Institute, Guiyang 550014, China

Received 10 March 2024; accepted 10 December 2024

Abstract: The impact of Y content on the microstructure, mechanical properties, and electromagnetic interference shielding effectiveness (EMI SE) of the Mg−6Zn−*x*Y−1La−0.5Zr alloy was investigated. After the extrusion treatment of Mg−6Zn−*x*Y−1La−0.5Zr alloy, the large grains that did not experience dynamic recrystallization were elongated along the extrusion direction, and the small-sized dynamic recrystallized grains were distributed around the large grains. The Mg−6Zn−1Y−1La−0.5Zr alloy demonstrated a favorable balance between strength and plasticity, exhibiting ultimate tensile strength, yield strength, and elongation values of 332.3 MPa, 267.3 MPa, and 16.2%, respectively. Moreover, the EMI SE within the frequency range of 30−1500 MHz changes from 79 to 110 dB, aligning with the electromagnetic shielding requirements of many high-strength applications.

Key words: Mg−Zn−Y−La−Zr alloys; dynamic recrystallization; microstructure; mechanical properties; electromagnetic interference shielding effectiveness

1 Introduction

Mg alloys, being the lightest materials for structural purposes, hold tremendous potential for application in aerospace and automotive industries, among others. In recent years, the research community has increasingly focused on exploring the functional and mechanical properties of Mg alloys. For instance, Mg alloys exhibit properties such as damping, flame retardance, thermal conductivity, and electromagnetic interference shielding effectiveness (EMI SE) [1,2]. However, there is a degree of mutual checks and balances between the mechanical and functional properties of Mg alloys. For example, the service environment of airborne radar reflector sheets is complex and dynamic, and in addition to the need for high mechanical properties, high EMI SE is also a crucial performance indicator [3]. Consequently, the synergistic optimization of the mechanical properties and EMI SE of Mg alloys has become an urgent challenge.

Numerous researchers have endeavored to enhance the mechanical properties of Mg alloys [4−6]. It has been well-established that alloying combined with hot deformation is an effective means to improve the mechanical properties of Mg alloys. For instance, under the same extrusion conditions, Mg−3Ag alloys exhibited a 137% strength enhancement compared to pure Mg [7]. LI et al [8] incorporated varying amounts of Ca element into Mg−3.8Al−1.1Sn alloys in combination with asymmetric severe shear extrusion (ASSE), which resulted in Mg−3.8Al−1.1Sn−0.4Ca sheets with a desirable combination of

Corresponding author: Xian-hua CHEN, Tel: +86-15922784658, E-mail: xhchen@cqu.edu.cn
https://doi.org/10.1016/S1003-6326(25)66906-8

high strength (ultimate tensile strength (UTS) of ~320 MPa, yield strength (YS) of ~220 MPa) and ductility (elongation of ~18.0%). In recent years, rare earth (RE) elements, such as Y, have been recognized as effective strengthening agents in Mg alloys, as they can form a large number of RE compound phases to achieve excellent secondary phase strengthening. CHANG et al [9] investigated the addition of different Y contents to Mg−4Li−3Al alloys, demonstrating that Y addition significantly enhances the mechanical properties of Mg alloys, with the extruded Mg−4Li−3Al−1.5Y alloy exhibiting an UTS of ~248 MPa and an elongation of ~27%. They attributed this improvement to the grain refinement, solid solution strengthening, and precipitation strengthening effects induced by the Y addition. Furthermore, LEI et al [10] showed that the addition of Y to Mg alloys would favor the activation of pyramidal slip, leading to enhanced ductility, as evidenced by the excellent ductility of the Mg−4Gd−0.5Zr−*x*Y alloys. Collectively, the research suggests that Y may be a key element in synergizing the strength and plasticity of Mg alloys.

A recent review of the EMI SE of Mg alloys has indicated the occurrence of three types of loss mechanisms when electromagnetic waves penetrate a material: reflection loss on the material's surface, absorption loss due to electromagnetic-induced eddy currents within the material, and multiple reflection loss at interfaces with different impedances [11]. The extent of reflection and absorption loss are highly dependent on the electrical conductivity of the material. Hence, the primary approach for developing high EMI SE Mg alloys is to incorporate low solid solubility elements, which reduce lattice distortion and enhance the electrical conductivity of the material. Conversely, multiple reflection loss primarily occurs at interfaces with varying impedance within the material; the more the number of interfaces, the greater the likelihood of reflection of electromagnetic waves on the material surface. In our previous study, we constructed a spatial cage-type secondary phase distribution in the Mg−12Gd−3Y−1.5Nd alloy, resulting in an 80−112 dB SE within the frequency range of 30−1500 MHz [12]. This has been confirmed by numerous similar studies [13−15]. Controlling the solid solubility and providing more secondary phase interfaces are effective means of improving the EMI SE of Mg alloys. Y can form a large number of RE compound phases in Mg alloys, which in turn provide more secondary phase interfaces for the reflection of electromagnetic waves. Despite the large solid solubility of Y in Mg alloys, adding a lower Y content does not appear to have a significant negative impact on the EMI SE of Mg alloys [16].

In our previous studies, we incorporated 1 wt.% Y or La element separately into the ZK60 (Mg−6Zn−0.5Zr) alloy, followed by extrusion and rolling processes to produce sheets with exceptional mechanical properties and EMI SE [17,18]. In this study, we focused on the Mg−6Zn−1La−0.5Zr alloy as the matrix to examine the impact of varying Y contents on the microstructure, mechanical properties, and EMI SE of the extruded sheets. This study will promote the development of structure function integrated Mg alloys.

2 Experimental

Commercially purchased high-purity Mg ingots, pure Zn, Mg−30wt.%Y intermediate alloy, Mg−30wt.%La intermediate alloy, and Mg−30wt.%Zr intermediate alloy were fed sequentially into a high frequency induction melting furnace at 750 °C in the specified ratio (*x*=0, 0.5, 1.0 and 1.5 wt.%) and melted under a protective atmosphere consisting of CO_2 and SF_6 with a volumetric ratio of 99∶1.

After adding the alloy raw materials at each step, the temperature was maintained at approximately 750 °C for 20 min. Once the raw materials were completely melted, the slag was removed from the crucible, and the crucible was slowly placed in water using a clamp to obtain an ingot diameter of 130 mm. During the cooling process, a protective gas was continuously vented to the surface of the melt to insulate it from oxygen. The chemical composition of the ingot was determined using a fluorescence analyzer (XRF−1800 CCDE) at its center, as presented in Table 1. Subsequently, the ingots underwent homogenization in a chamber heat treatment furnace at 400 °C for 12 h. Removing the surface oxide layer resulted in a homogenized billet with a diameter of 125 mm. The homogenized billet and the extrusion die were preheated in a resistance furnace at 390 °C for 2 h prior to the extrusion process.

Table 1 Chemical compositions of ZKL601−*x*Y alloy (wt.%)

Designed composition	Abbreviation	Analyzed composition				
		Mg	Zn	Y	La	Zr
Mg−6Zn−1La−0.5Zr	ZKL601	Bal.	6.22	0	0.96	0.48
Mg−6Zn−0.5Y−1La−0.5Zr	ZKL601−0.5Y	Bal.	5.98	0.52	1.17	0.57
Mg−6Zn−1Y−1La−0.5Zr	ZKL601−1.0Y	Bal.	6.13	0.98	1.09	0.54
Mg−6Zn−1.5Y −1La−0.5Zr	ZKL601−1.5Y	Bal.	6.31	1.46	1.24	0.46

The extrusion process was carried out at a temperature of 390 °C with an extrusion ratio of 11∶1. Mg alloy plates with dimensions of 140 mm in width and 8 mm in thickness were obtained.

Microstructure observation in this work was conducted on the extrusion direction−transverse direction (ED−TD) plane. Surface morphology and secondary phase distribution characteristics of the samples were observed using an optical microscope. Optical microscopy (OM) and scanning electron microscopy (SEM) observations were performed after the samples underwent stepwise polishing on SiC sandpaper and conventional mechanical polishing using a picric acid etchant to etch the grain boundaries. The physical phase information of the as-cast and extruded alloys was determined using an X-ray diffractometer (Rigaku d/maX−2500PC) operated at 60 kV. The XRD scanning range was 10°−90° with a step size of 0.02 (°)/min. Grain orientation, recrystallization degree, and structure of the extruded alloys were measured using electron backscatter diffraction (EBSD) on a scanning electron microscope equipped with an EBSD probe. The samples used for EBSD testing were prepared from the extruded alloys. Prior to testing, the samples were electrolytically polished in AC-II electrolyte for 1.5 min at a voltage of 20 V and a current of 0.2 A. The EBSD test results were analyzed using Aztec Crystal software. Additionally, transmission electron microscopy (TEM, FEI TECNAI G2 F20) was used to observe the secondary phase characteristics of typical specimens. The mechanical properties of the samples were determined using a CMT−5105 universal mechanical material testing machine. For each state, three dog-bone-shaped tensile specimens were cut along the ED direction. Each specimen underwent three repeated tensile tests, and the average value was calculated. The electromagnetic shielding properties of the alloys were evaluated according to the ASTM D4935—2010 standard coaxial cable method within the frequency range from 30 to 1500 MHz.

3 Results

3.1 Microstructure of as-cast alloy

Figure 1 displays the SEM images of the as-cast ZKL601−*x*Y alloys. The microstructure of the as-cast ZKL601−*x*Y alloys displays a consistent dendritic morphology, with eutectic phases distributed along the grain boundaries. The variation in Y content does not significantly affect the microstructure morphology of the as-cast alloy. The high magnification of the ZKL601−*x*Y alloys' microstructure reveals that an increased Y content refines the grain size. This refinement is primarily attributed to the aggregation of rare-earth (RE) atoms at the solid−liquid interface during the solidification. Y has low solid solubility in Mg, so its addition enriches RE compounds at the grain boundaries. The high melting point compounds impede dendrite growth, making the alloys more prone to dendritic growth, resulting in a noticeable refinement of the alloy grains [19]. As the Y element content gradually increases, the reticulated eutectic phase at the grain boundaries coarsens, and a portion of the secondary phases spread towards the grain interior due to composition supercooling. The SEM images and the high-magnification morphology reveal that the eutectic phase in the as-cast ZKL601 alloy without Y is distributed in a discontinuous mesh structure, with a few granular secondary phases within the grains. When the Y element content exceeds 1.0 wt.%, the morphology of the secondary phases at the grain boundaries transforms from a discontinuous mesh to a continuous mesh, with a gradually increasing density as the Y content increases. At a Y content of 1.5 wt.%, the secondary phase at the grain boundaries transforms into a continuous mesh, with a progressively higher density as the Y content rises.

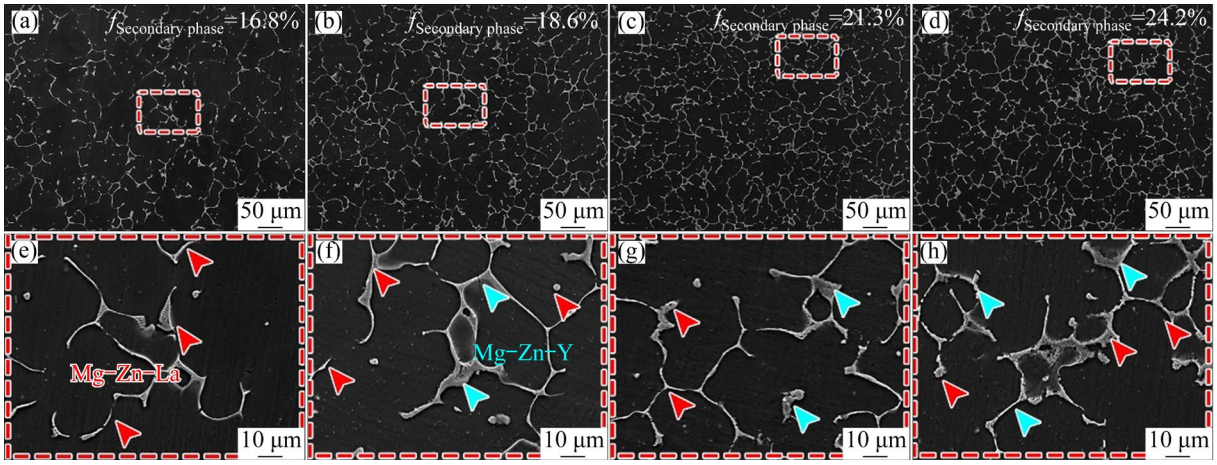

Fig. 1 SEM images of as-cast ZKL601−*x*Y alloys: (a, e) ZKL601; (b, f) ZKL601−0.5Y; (c, g) ZKL601−1.0Y; (d, h) ZKL601−1.5Y ((e, f, g, h) are enlarged images of red boxes in (a, b, c, d), respectively)

Beyond a Y content of 1.5 wt.%, a substantial quantity of RE-rich phases accumulate at the grain boundaries, resulting in a more pronounced coarsening of these boundaries. Concurrently, the fine-grained phases within the grains gradually diminish. Based on XRD patterns (Fig. 2) and previous findings, RE-rich phases predominantly constitute the secondary phase distributed along the grain boundaries of the ZKL601−*x*Y alloy [17,18]. The Mg−Zn−Y phase (a combination of Mg_3YZn_6 and $Mg_3Y_2Zn_3$ phases) is primarily distributed as layered structures where the grain boundaries intersect. In contrast, the Mg−Zn−La phase appears as either block-like or elongated strip-like features at the grain boundaries, and these two phases exhibit a mutually dependent growth relationship.

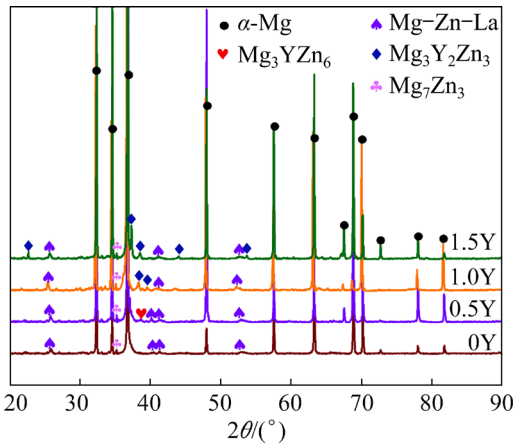

Fig. 2 XRD patterns of as-cast ZKL601−*x*Y alloys

3.2 Microstructure of extruded alloy

Figure 3 displays the OM and SEM images of the ZKL601−*x*Y alloys after extrusion treatment. The ZKL601−*x*Y alloys underwent a noticeable dynamic recrystallization (DRX) process after extrusion treatment. Likewise, the overall microstructures of the ZKL601−*x*Y alloys after extrusion display a bimodal microstructure, characterized by the coexistence of large and small grains. The coarse grains that did not undergo DRX elongated along the ED, while small-sized DRXed grains were distributed around larger grains, forming a necklace-like structure. SEM images reveal that the secondary phase of the as-cast alloy, which was localized along the grain boundaries of the RE-rich alloy mesh, experienced deformation under the applied extrusion pressure. The secondary phase gradually migrated and flowed in the ED, aligning itself with the ED. Higher magnification SEM images reveal that these particulate phases are primarily concentrated along the grain boundaries. The volume fraction of the secondary phase in the extruded ZKL601−*x*Y alloy was determined using the Image Pro Plus software. The results indicate that as the Y content in the ZKL601−*x*Y alloys increases, the volume fraction of the granular phase in the extruded alloy also increases, consistent with the statistical trend observed in the as-cast alloy. XRD patterns (Fig. 4) indicate that the primary secondary phases present in the ZKL601−*x*Y alloys after extrusion are Mg−Zn−Y, Mg−Zn−La, and Mg−Zn phases. Previous studies [17,18] have shown that the Mg−Zn−Y and Mg−Zn−La phases are secondary phases with a granular micrometer-scale structure, while the Mg−Zn phase exhibits a nanoscale structure. It is evident from the SEM field of view in Fig. 3 that the granular secondary

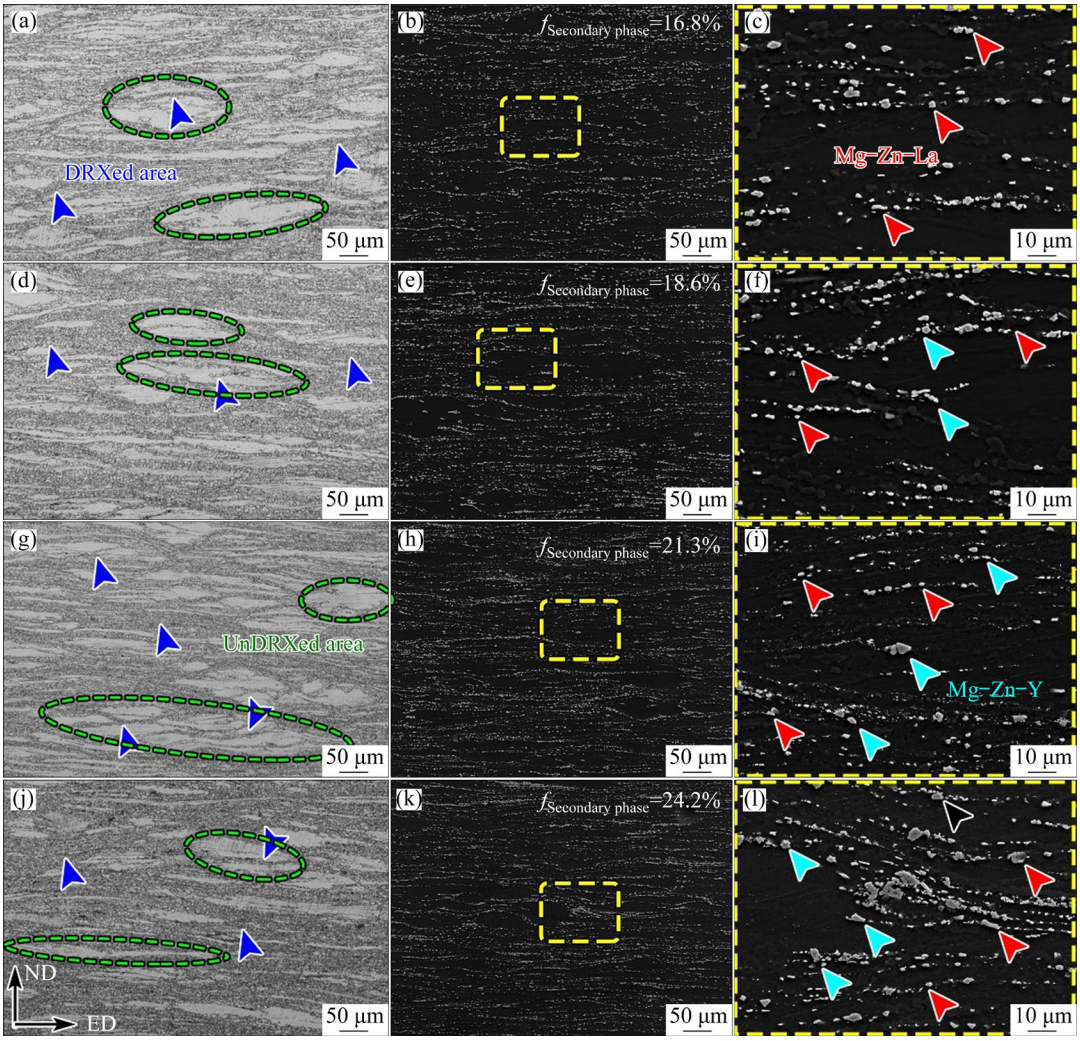

Fig. 3 OM (a, d, g, j) and SEM (b, c, e, f, h, i, k, l) images of extruded ZKL601−xY alloys: (a−c) ZKL601; (d−f) ZKL601−0.5Y; (g−i) ZKL601−1.0Y; (j−l) ZKL601−1.5Y ((c, f, i, l) are enlarged images of yellow boxes in (b, e, h, k), respectively)

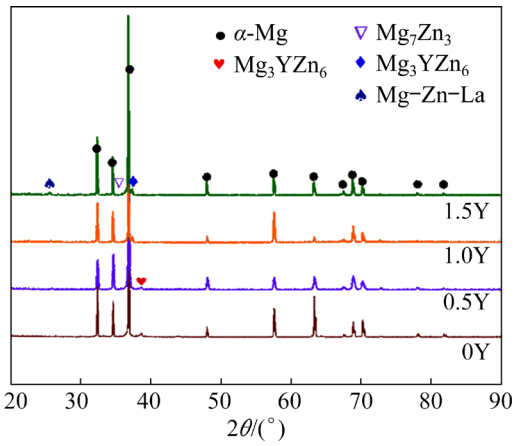

Fig. 4 XRD patterns of extruded ZKL601−xY alloys

phase primarily consists of the Mg−Zn−Y and Mg−Zn−La phases [17,18]. However, the nanoscale Mg−Zn phase is challenging to observe within the SEM field of view.

To further identify the secondary phase species present in the ZKL601−xY alloys after extrusion, including the Mg−Zn phase that is challenging to observe under SEM, TEM observation was conducted on the ZKL601−1Y alloy, which exhibited the best mechanical properties. Figure 5 illustrates the TEM results of the ZKL601−1.0Y alloy in the extruded state. Evidently, in line with the XRD analysis results, the secondary phase in the extruded ZKL601−1.0Y alloy primarily consists of micrometer-scale Mg−Zn−La, Mg−Zn−Y, and some nanoscale Mg−Zn phases. Importantly, little dislocation motion is observed near the Mg−Zn−La and Mg−Zn−Y phases, providing evidence that these phases effectively reinforce the alloy by impeding dislocation motion.

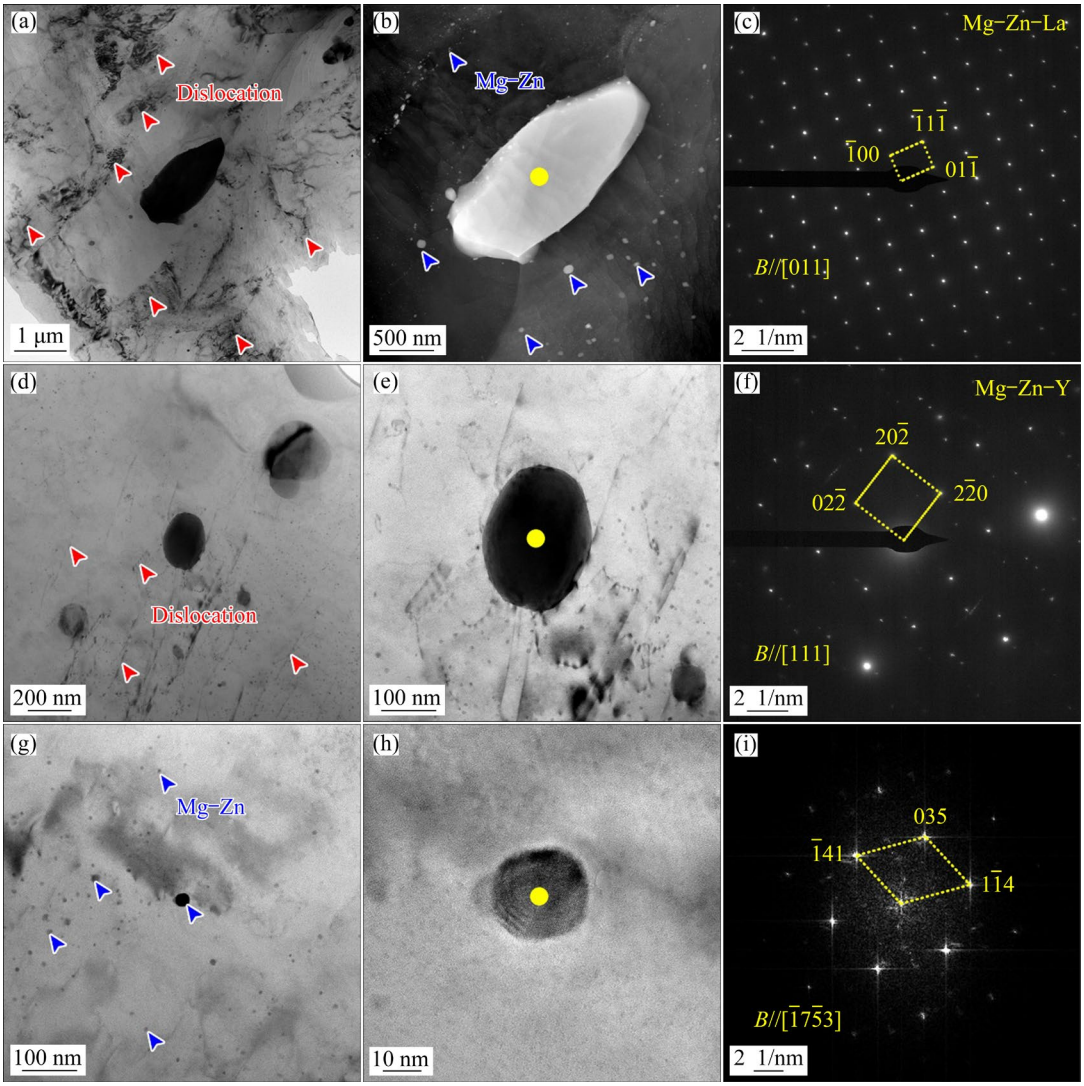

Fig. 5 TEM images and SAED patterns of extruded ZKL601−1.0Y alloy with different secondary phases: (a, d, e, g, h) BF TEM image; (b) HAADF TEM image; (c) SAED pattern corresponding to plate-like particle in (b); (f) SAED pattern corresponding to circular particle in (e); (i) SAED pattern corresponding to particle in (h)

In this study, the grain orientation spread (GOS) values were utilized to classify the grains in the ZKL601−*x*Y alloys into three categories: DRXed grains (GOS < 2), less deformed grains after recrystallization (substructures) (2 < GOS< 5), and deformed grains (GOS > 2) [20]. Figure 6 presents the inverse pole figure (IPF) of the DRXed grains, substructures, and deformed grains of the ZKL601−*x*Y alloys after extrusion. Consistent with the OM observations, the microstructures of the ZKL601−*x*Y alloys, once extrusion is completed, exhibit a bimodal microstructure characterized by the coexistence of deformed large grains and DRXed small grains. The coarse grains that did not undergo DRX were elongated along the ED, while the small-sized DRXed grains were distributed around the large grains. The volume fractions of DRXed grains, substructures, and deformed grains were subsequently calculated. Interestingly, the volume fractions of DRXed grains, substructures, and deformed grains did not exhibit a monotonically increasing or decreasing trend after extrusion of the ZKL601−*x*Y alloys. Specifically, the volume fractions of DRXed grains in the ZKL601−*x*Y alloys at *x*=0, 0.5, 1.0 and 1.5 are 48.6%, 49.6%, 49.6%, and 49.6%, respectively. This phenomenon demonstrates that the increase in Y content still promotes the increase of DRX volume fraction to some extent, with the highest DRX volume fraction being achieved in the ZKL601−1.0Y alloy. In contrast to the statistical results for the degree of DRX, the substructure of

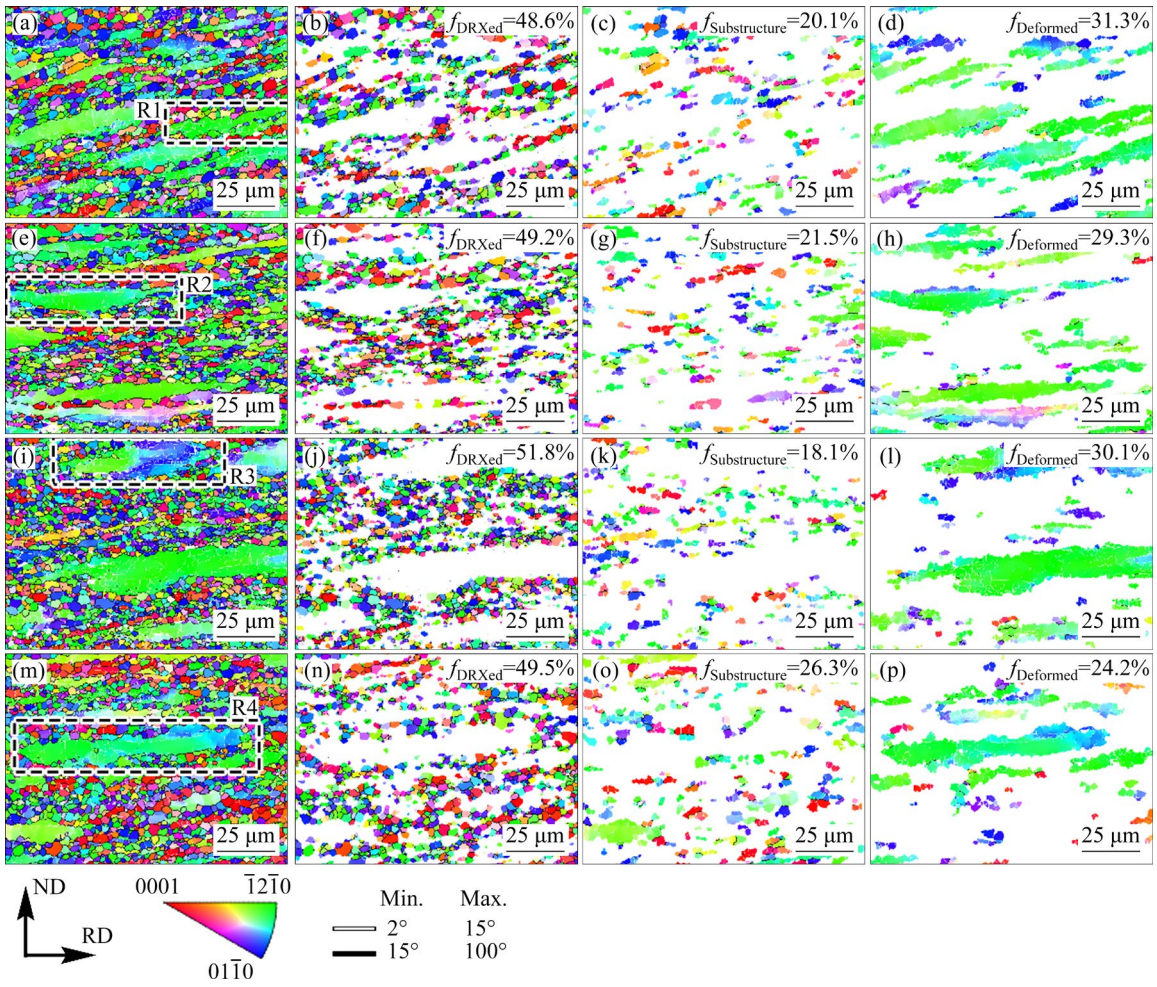

Fig. 6 IPF maps of extruded ZKL601−*x*Y alloys: (a−d) ZKL601; (e−h) ZKL601−0.5Y; (i−l) ZKL601−1.0Y; (m−p) ZKL601−1.5Y; (a, e, i, m) All grains; (b, f, j, n) DRXed grains; (c, g, k, o) Substructures; (d, h, l, p) Deformed grains

the ZKL601−*x*Y alloys in the extruded state shows significant differences in deformed grain proportions. The volume fractions of the substructures of the ZKL601−*x*Y alloys at *x*=0, 0.5, 1.0, and 1.5 after extrusion completion are 20.1%, 21.5%, 18.1%, and 26.3%, respectively, exhibiting fluctuations of increasing, then decreasing, and finally increasing. Correspondingly, the deformed grain proportions of the other three alloys fluctuated around 30%, except for the ZKL601−1.5Y alloy, which had a significantly lower deformed grain proportion compared to the other three alloys.

The average grain size distributions of all grains, DRXed grains, substructures, and deformed grains of the ZKL601−*x*Y alloys after extrusion are statistically presented in Fig. 7. It is evident from the results that the average grain sizes of the ZKL601−*x*Y alloys at *x*=0, 0.5, 1.0, and 1.5 are 2.70, 2.43, 2.10, and 2.44 μm, respectively, after the completion of extrusion. These values exhibit a trend of decreasing and then increasing with the increase of the Y content. Notably, the ZKL601−1.0Y alloy achieved the smallest average grain size. When considering the average grain sizes of DRXed grains, substructures, and deformed grains, the ZKL601−*x*Y alloys displayed values of 2.28, 2.09, 1.85, and 2.08 μm, respectively, after extrusion completion. It is observed that the addition of Y in the ZKL601−*x*Y alloy initially led to a decrease in the grain size of DRXed grains, followed by an increase. However, overall, the inclusion of Y in the ZKL601−*x*Y alloy promoted the refinement of DRXed grains. The most pronounced refinement in DRX grain size was achieved when the alloy contained 1.0 wt.% Y. Similarly, the grain sizes of the substructure and

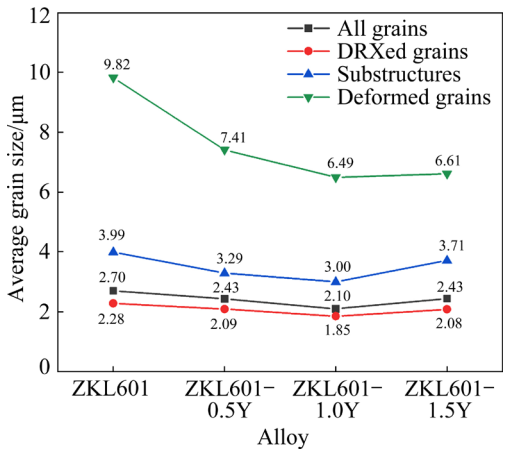

Fig. 7 Average grain size distributions of all grains, DRXed grains, substructures, and deformed grains of extruded ZKL601−*x*Y alloys

deformed grains of the ZKL601−*x*Y alloy after extrusion exhibited trends consistent with the changes in DRX grain size, both displaying a pattern of decreasing and then increasing. The finest DRXed and deformed grains were observed in the ZKL601−1.0Y alloy. Macroscopically, the average grain size of the ZKL601−1.0Y alloy was slightly smaller than that of the other three alloys after the completion of extrusion.

Further observation of the (0001) basal texture and pole figure (PF) of the ZKL601−*x*Y alloys after extrusion is shown in Fig. 8. The highest density point of the (0001) basal texture of the ZKL601−*x*Y alloys after extrusion is located near the TD axis, and the majority of grains exhibit a perpendicular orientation of their *c*-axis to the ED−ND plane. This demonstrates prominent extrusion texture characteristics, as well as the distinct separation of DRXed grains, substructures, and the (0001) basal texture of deformed grains. The DRXed grains display random orientations, resulting in a significant orientation gradient across the (0001) basal texture, spanning almost the entire ND axis

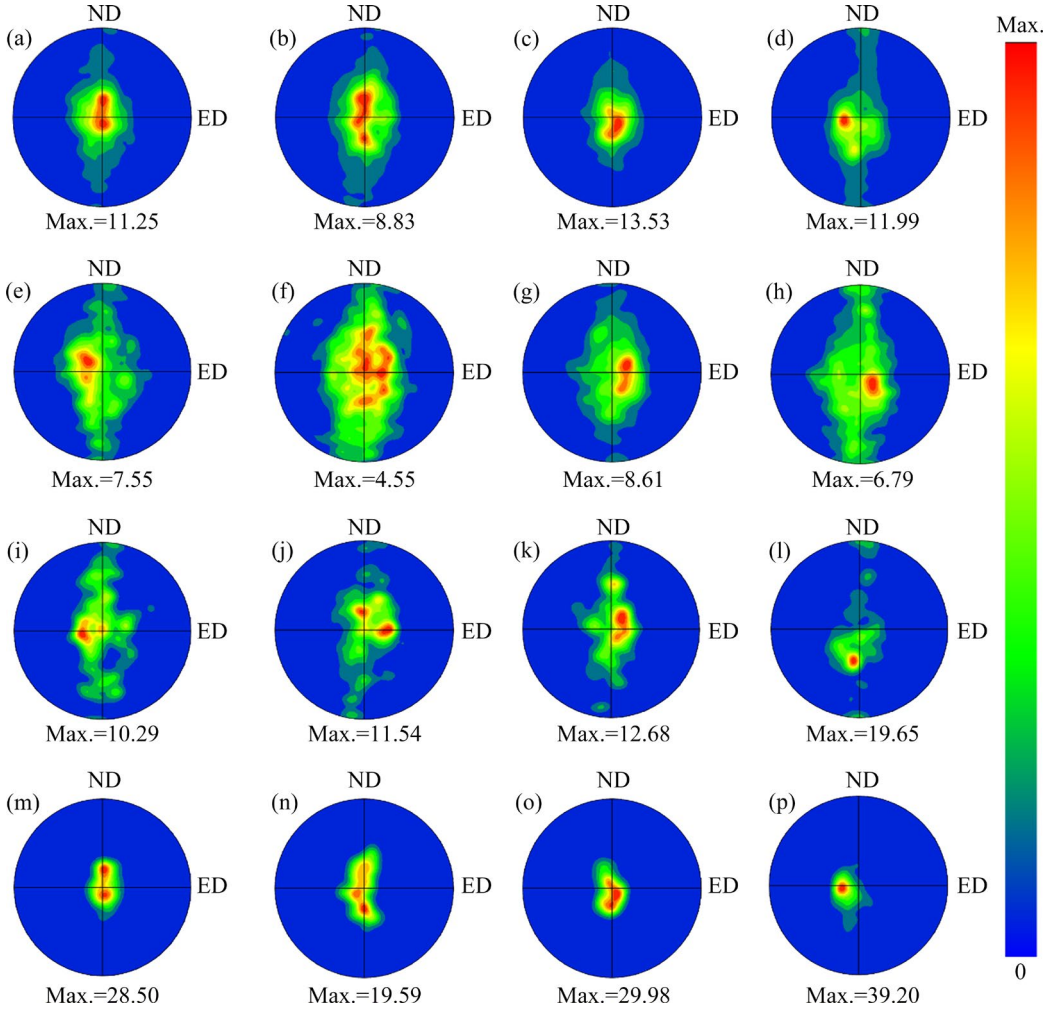

Fig. 8 PFs of extruded ZKL601−*x*Y alloys: (a−d) ZKL601; (e−h) ZKL601−0.5Y; (i−l) ZKL601−1.0Y; (m−p) ZKL601−1.5Y; (a, e, i, m) All grains; (b, f, j, n) DRXed grains; (c, g, k, o) Substructures; (d, h, l, p) Deformed grains

and extending prominently in the ED. Similarly, the substructures exhibit an extensive orientation gradient on the (0001) basal texture, although slightly more concentrated compared to the DRXed grains. Interestingly, the deformed grains show a remarkable concentration of orientation on the (0001) plane. With an increase in Y content in the ZKL601−*x*Y alloys, the strength of the (0001) basal texture displays a trend of decreasing, then increasing, and finally decreasing again. However, the (0001) basal textures of the ZKL601−1.0Y and ZKL601−1.5Y alloys are noticeably contracted compared to the ZKL601 alloy. This phenomenon is closely linked to the concentrated orientation of the deformed grains in the ZKL601−1.0Y and ZKL601−1.5Y alloys. The basal texture strengths of the deformed grains in the ZKL601−1.0Y and ZKL601−1.5Y alloys reach surprisingly high values of 29.98 and 39.20, respectively.

The IPF maps of the ZKL601−*x*Y alloys after extrusion deformation are shown in Fig. 9. The highest texture strength is observed in the $(01\bar{1}0)$ plane. As the Y content increases from 0 to 0.5, 1.0, and 1.5 wt.%, there is a trend of increasing and then decreasing texture strengths, with values of 5.19, 6.07, 5.48, and 3.99, respectively. Upon further examination of the IPF of DRXed grains, substructures, and deformed grains, it is observed that the strongest texture strength of IPF among the DRXed grains in the ZKL601−*x*Y alloys without Y element is observed in the $(01\bar{1}0)$ plane. However, in the ZKL601−*x*Y alloy with the addition of Y, the IPF maps of the DRXed grains are observed in the $(01\bar{1}0)$ and $(\bar{1}2\bar{1}0)$ planes. This indicates a shift in the texture pattern of the DRXed grains from the $(01\bar{1}0)$ to the $(\bar{1}2\bar{1}0)$ planes in the ZKL601−*x*Y alloy when Y is added. In contrast, the IPF maps of the substructures exhibit opposite characteristics to those of the DRXed grains. This demonstrates that the Y addition significantly promotes the transformation of the texture pattern of the DRXed grains from the $(01\bar{1}0)$ to the $(\bar{1}2\bar{1}0)$ planes in the ZKL601−*x*Y alloy.

The microstructures of the ZKL601−*x*Y alloys after extrusion show typical bimodal characteristics. However, there are no significant differences in the average grain size, DRX volume fraction, and texture strength components of the extruded ZKL601−*x*Y alloys. The results of the kernel average misorientation (KAM) analysis of the ZKL601−*x*Y alloys in the extruded state are presented in Fig. 10. Similarly, the average KAM values of the extruded ZKL601−*x*Y alloys do not

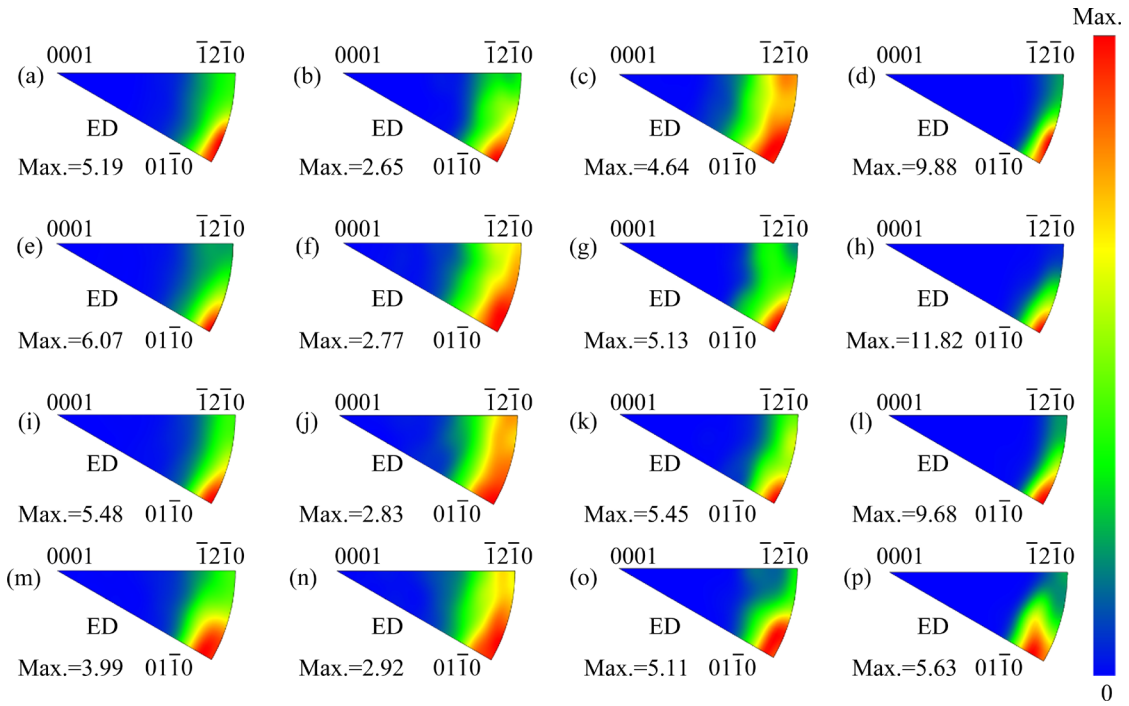

Fig. 9 IPF maps of extruded ZKL601−*x*Y alloys: (a–d) ZKL601; (e–h) ZKL601−0.5Y; (i–l) ZKL601−1.0Y; (m–p) ZKL601−1.5Y; (a, e, i, m) All grains; (b, f, j, n) DRXed grains; (c, g, k, o) Substructures; (d, h, l, p) Deformed grains

exhibit a direct correlation with the Y content. The extruded ZKL601−*x*Y alloys demonstrate the highest KAM value. Upon further examination of the KAM values of the DRXed grains, substructures, and deformed grains, it is observed that among the four alloys, the DRXed grains display the lowest KAM values, the substructures exhibit intermediate KAM values, and the larger deformed grains show the highest KAM values. To some extent, the KAM values can indicate the degree of strain in the deformed regions and the density of local dislocations. It can be inferred that the ZKL601−*x*Y alloys accumulate significant residual stresses and dislocations in the deformed grains that remain after extrusion.

In contrast, the overall KAM value of the DRXed grains is lower, indicating more complete internal deformation in these grains with a small accumulation of dislocations. It should be noted that although the DRXed grains are more extensively deformed and exhibit lower KAM values overall, localized regions still display higher KAM values. To some extent, this phenomenon suggests that the newly formed DRX grains in the ZKL601−*x*Y alloys still undergo some level of deformation during the extrusion process and accumulate a small number of dislocations in these regions.

Figure 11 illustrates the Schmidt factors (SFs) for basal ⟨*a*⟩ slip, prismatic ⟨*a*⟩ slip, pyramidal ⟨*a*⟩ slip, and pyramidal ⟨*c*+*a*⟩ slip systems in the extruded state of the ZKL601−*x*Y alloys. Overall, the SFs for prismatic ⟨*a*⟩ slip, pyramidal ⟨*a*⟩ slip, and pyramidal ⟨*c*+*a*⟩ slip of the extruded ZKL601−*x*Y alloys do not exhibit significant differences and all display high values, indicating substantial slip activity in these modes. However, the activation of non-basal slip is challenging and

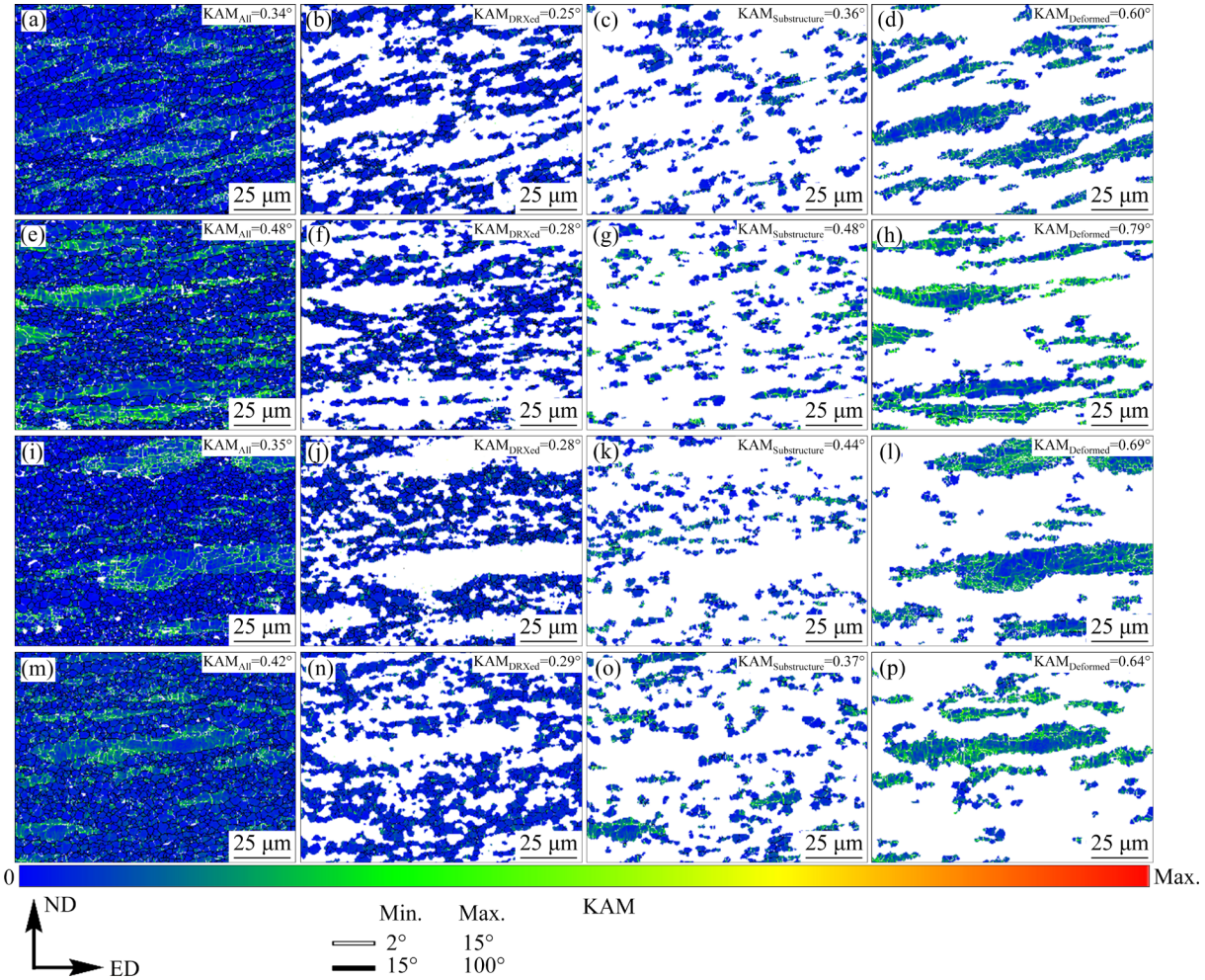

Fig. 10 KAM values of extruded ZKL601−*x*Y alloys: (a−d) ZKL601; (e−h) ZKL601−0.5Y; (i−l) ZKL601−1.0Y; (m−p) ZKL601−1.5Y; (a, e, i, m) All grains; (b, f, j, n) DRXed grains; (c, g, k, o) Substructures; (d, h, l, p) Deformed grains

coordinating deformation, particularly at room temperature, due to its higher critical resolved shear stress (CRSS). Furthermore, it is noteworthy that the basal SFs of the extruded ZKL601−*x*Y alloy at *x*=0, 0.5, 1.0, and 1.5 are 0.17, 0.17, 0.16, and 0.19, respectively, with a maximum deviation of only 0.03. Mg alloys primarily rely on basal slip to accommodate strains during room temperature deformation, and the stronger fiber texture in the extruded ZKL601−*x*Y alloy restricts the activation of basal slip by confining it to a specific orientation.

3.3 Mechanical properties

The room temperature mechanical tensile curves of ZKL601−*x*Y alloys in extruded state are shown in Fig. 12. The corresponding mechanical properties values are statistically shown in Table 2. The UTS values of ZKL601, ZKL601−0.5Y, ZKL601−1.0Y and ZKL601−1.5Y alloys in the extruded state are 295.2, 296.4, 332.3 and 298.5 MPa, and the YS values are 215.3, 218.2, 267.3 and 221.3 MPa, respectively. It can be seen that except for the ZKL601−1.0Y alloy, which has significantly better UTS and YS than the other three alloys, there is no significant difference in the UTS and YS of extruded ZKL601, ZKL601−0.5Y, and ZKL601−1.5Y alloys, all within the error range of tensile measurement. Unlike UTS and YS, the elongation of ZKL601−*x*Y alloys in extruded state decreases gradually with the increase of Y content. The extruded ZKL601−1.5Y alloy has the lowest elongation of 13.3%. Compared to the extruded

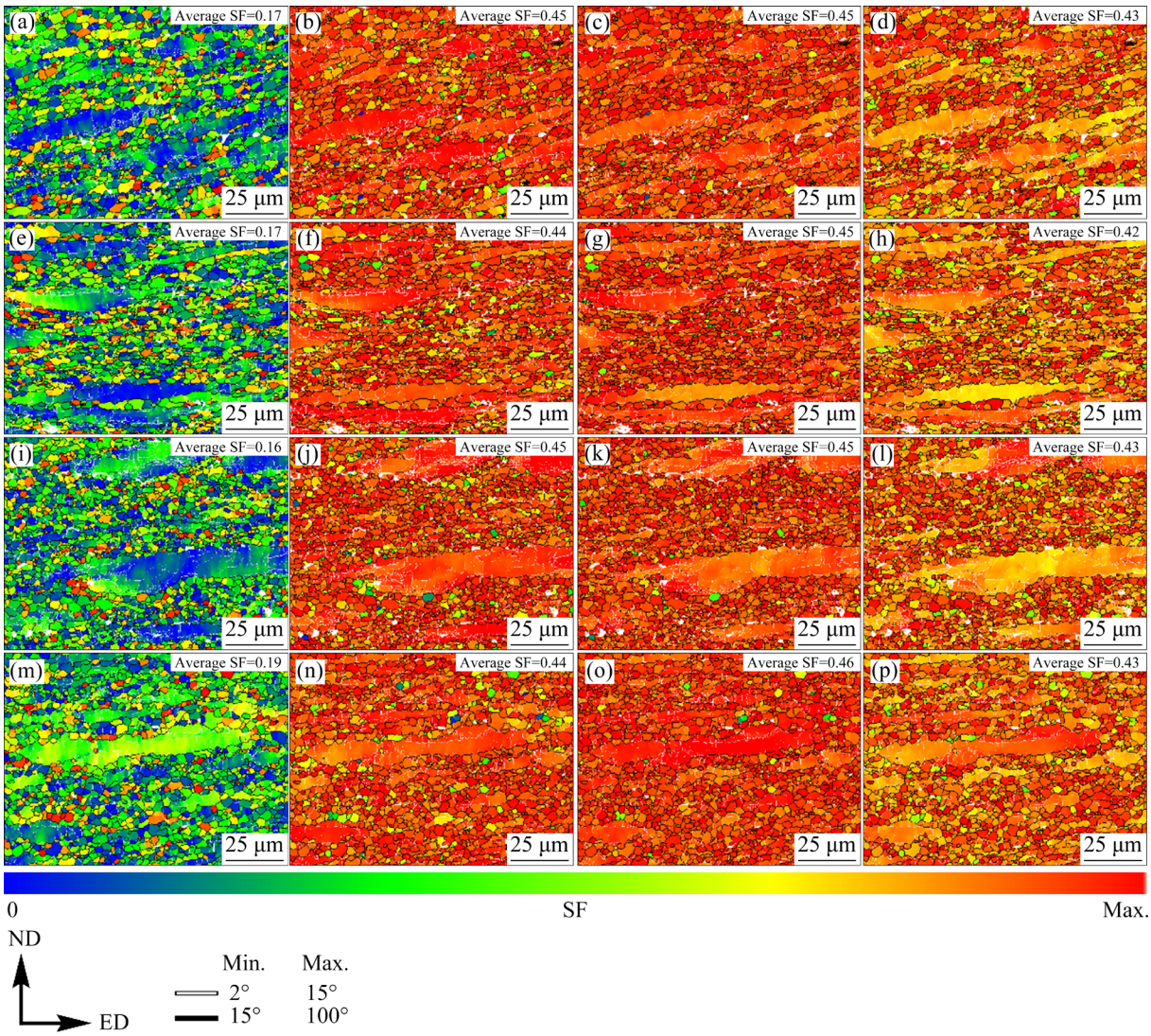

Fig. 11 SF factors of different slip modes in extruded ZKL601−*x*Y alloys: (a−d) ZKL601; (e−h) ZKL601−0.5Y; (i−l) ZKL601−1.0Y; (m−p) ZKL601−1.5Y; (a, e, i, m) Basal ⟨*a*⟩ slip; (b, f, j, n) Prismatic ⟨*a*⟩ slip; (c, g, k, o) Pyramidal ⟨*a*⟩ slip; (d, h, l, p) Pyramidal ⟨*c*+*a*⟩ slip

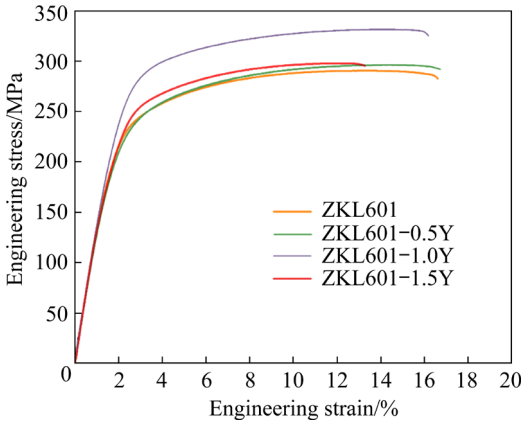

Fig. 12 Engineering stress−strain curves of ZKL601−*x*Y alloys after extrusion

Table 2 Mechanical properties of extruded ZKL601−*x*Y alloys

Alloy	UTS/MPa	YS/MPa	Elongation/%
ZKL601	295.2±5.7	215.3±6.2	21.7±0.3
ZKL601−0.5Y	296.4±4.8	218.2±3.7	19.9±0.3
ZKL601−1.0Y	332.3±3.5	267.3±2.8	16.2±0.4
ZKL601−1.5Y	298.5±4.2	221.3±5.1	13.3±0.2

ZKL601 alloy, the elongation decreases by 8.4%. It can be seen that ZKL601−1.0Y alloy obtains a superior balance of strength and plasticity, with UTS, YS and elongation of 332.3 MPa, 267.3 MPa and 16.2%, respectively. Compared with the extruded ZKL601 alloy, the UTS and YS are significantly higher, especially the YS, which is nearly 52.0 MPa.

3.4 Electromagnetic interference shielding effectiveness

The EMI SE curves of the extruded ZKL601−*x*Y alloy in the frequency range of 30−1500 MHz are shown in Fig. 13. The corresponding EMI SE values as well as the conductivity statistics are shown in Table 3. The conductivities of ZKL601, ZKL601−0.5Y, ZKL601−1.0Y, and ZKL601−1.5Y alloys in extruded state are 29.5%(IACS), 29.9%(IACS), and 30.2%(IACS), 30.2%(IACS), respectively, and the conductivities increase gradually with the increase of Y content. The EMI SE of ZKL601−*x*Y alloys in the extruded state shows a decreasing trend with the increase in test frequency. The EMI SE rises with the increase of Y content, and the EMI SE reaches the best when the Y element addition is 1.5 wt.%. The increase of Y content in ZKL601−*x*Y alloys significantly enhances the EMI SE in the low frequency band, but almost does not have any improvement effect in the high frequency band. ZKL601−1.5Y alloy achieved the best EMI SE in the frequency range of 30−1500 MHz, ranging from 81−111 dB.

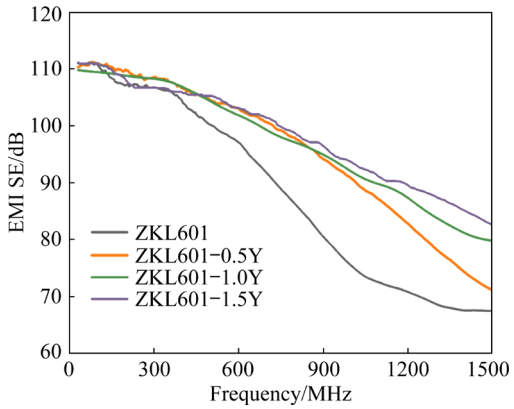

Fig. 13 EMI SE curves of ZKL601−*x*Y alloys after extrusion

4 Discussion

4.1 Role of Y content in tuning microstructure

The preceding microstructural analysis of the extruded ZKL601−*x*Y alloy reveals that alterations in the Y content of the ZKL601−*x*Y alloy lead to notable modifications in the microstructure of the extruded alloy. Moreover, an augmented Y content results in the introduction of a greater number of secondary phase particles, thereby facilitating a shift in the type of the DRXed texture.

The increase in Y content in the as-cast ZKL601−*x*Y alloy promotes the gradual coarsening of the reticulated eutectic structure at the pristine grain boundaries and its propagation towards the grain interior. Previous research has demonstrated that the reticulated eutectic phases formed in the as-cast ZKL601−*x*Y alloys exhibit high thermal stability and difficult to completely dissolve into the matrix during homogenization [21]. Consequently, these phases are progressively fragmented into granular forms under the extrusion force, exhibiting a distinct streamline distribution along the ED. The presence of these granular phases impedes the dislocation motion during extrusion, causing the accumulation of dislocations in their vicinity. Furthermore, the applied strain induces the generation of high-density lattice defects, including dislocations and vacancies, in the Mg alloy [22].

Table 3 Conductivity and EMI SE of extruded ZKL601−*x*Y alloys

Alloy	Conductivity/ %(IACS)	EMI SE range/dB	EMI SE/dB		
			800 MHz	1000 MHz	1.5 GHz
ZKL601	29.5	67−111	86	75	67
ZKL601−0.5Y	29.9	71−110	97	90	71
ZKL601−1.0Y	30.2	79−110	97	91	79
ZKL601−1.5Y	30.2	82−111	98	93	82

These defects promote solute diffusion, and provide nucleation sites and energy for the precipitation of nanoscale precipitates, leading to the dynamic formation of some nanoscale Mg−Zn phases in the ZKL601−1.0Y alloy.

The SEM images of the ZKL601−*x*Y alloys after extrusion reveal the generation of numerous DRXed grains near the granular phase, indicating the active occurrence of the PSN mechanism during hot extrusion. The presence of secondary phase particles larger than 1 μm in Mg alloys can contribute to DRX behavior through the PSN mechanism during hot deformation [23,24]. Additionally, the texture of the alloy is closely associated with the random orientation of DRX grains. The alteration of DRX texture components during the hot extrusion of the ZKL601−*x*Y alloys is intricately linked to the occurrence of PSN-induced DRX behavior. Previous studies have shown that Mg alloys primarily rely on discontinuous dynamic recrystallization (DDRX) and continuous dynamic recrystallization (CDRX) to complete the DRX process during the hot deformation [21,25]. DDRX typically occurs near grain boundaries due to the presence of lattice distortions, resulting in variations in dislocation density between neighboring grains. The deformed regions in Fig. 6 were examined using local magnification analysis, which revealed that the coarse deformed regions in R1, R2, R3, R4 completed the DRX process through nucleation at grain boundaries (the formation of sub-grains S1−S5 (Fig. 14) at the edge of the coarse grain region confirms this point). In addition to impeding dislocation motion through grain boundaries, the presence of fine secondary phase particles within the grains can also hinder dislocation motion and promote substructure development. TEM results in Fig. 5 indicate that the abundance of Mg−Zn phases within the grains of the extruded ZKL601−1.0Y alloy hinder the growth of sub-grains and stabilizes the orientation difference of sub-grain boundaries. These trapped sub-grain boundaries do not transform into DRXed grains and form deformed regions. However, it is important to note that despite the inhibitory effect of the abundant Mg−Zn phase on sub-grain boundary growth, some localized regions still initiate the formation of new DRXed grains without an obvious nucleation process, which is consistent with the CDRX feature. The successive changes in orientation difference within the deformed grains (e.g., Lines *AB*, *CD*, *EF*, and *GH*) and the abundance of sub-grain boundaries in Fig. 14 indicate the degree of activity of the CDRX mechanism.

The analytical results indicate that the coarse reticular eutectic phase in the ZKL601−1.0Y alloy undergoes a transition to a granular form during the extrusion. The granular secondary phase and original grain boundaries play a role in promoting the DRX process. However, the Mg−Zn phase that dynamically precipitates inside the grains due to strain induction inhibits the CDRX process. Figure 15 illustrates the distribution of orientation differences in the extruded ZKL601−*x*Y alloys. Since CDRX generally occurs inside the grains, the volume fraction of low-angle grain boundaries (LAGBs) within the grains can serve as an indicator of the level of CDRX activity. Increasing the Y content in the ZKL601−*x*Y alloys significantly reduces the occurrence of LAGBs. This suggests that a higher Y content inhibits the CDRX process and promotes the DDRX process. CDRX and DDRX both contribute to the grain refinement, and altering the Y content does not affect the underlying DRX mechanism. However, it is important to note that the DRX volume fraction of the extruded ZKL601−*x*Y alloys remains similar, while the substructure volume fraction exhibits significant differences. Specifically, in the ZKL601−1.5Y alloy, the substructure proportion reaches an astonishing 26.2%. This can be attributed to the fine dynamic

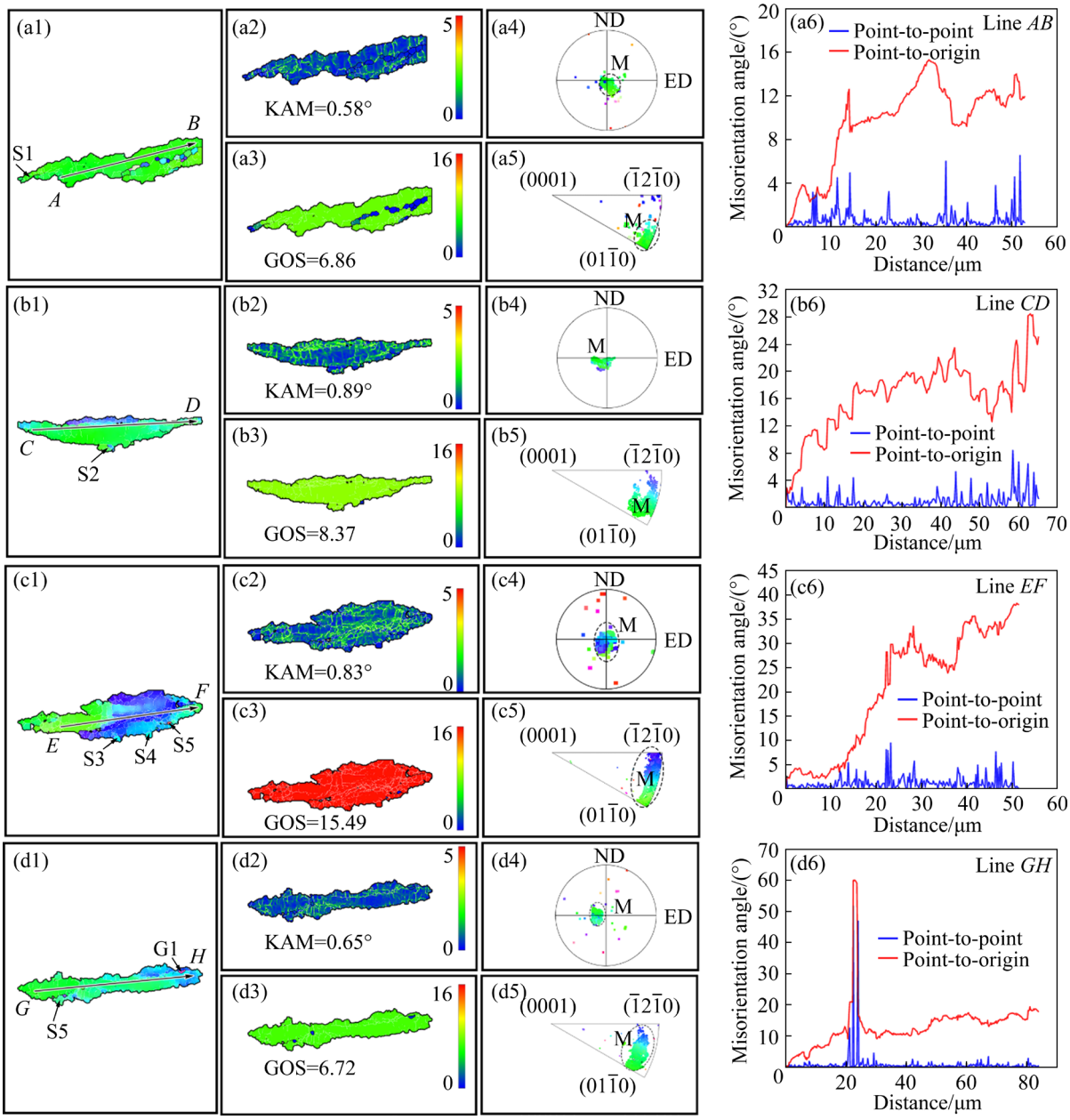

Fig. 14 Typical DDRX and CDRX regions selected in Fig. 6: (a1−a6) ZKL601; (b1−b6) ZKL601−0.5Y; (c1−c6) ZKL601−1.0Y; (d1−d6) ZKL601−1.5Y

precipitates inside the grains that trap the substructure boundaries during thermal deformation, hindering their transformation into DRX grains. Furthermore, the entrapment of substructure boundaries by the fine dynamic precipitates significantly influences the fraction of the DRXed texture, which explains the changes observed in the DRX and substructure texture fractions of the extruded ZKL601−*x*Y alloy.

4.2 Strengthening mechanisms of Y

The analysis presented in Fig. 12 shows the mechanical properties of the ZKL601−*x*Y alloys after extrusion. It is observed that, except for the ZKL601−1.0Y alloy, the YS of the other three alloys shows minimal variation after extrusion and falls within the range of experimental error. Conversely, the YS of the ZKL601−1.0Y alloy increases by approximately 52 MPa after extrusion. The properties of the material are determined by its microstructure, with grain size, secondary phase distribution, dislocation density, and texture being the primary factors influencing its strength. Specifically, in this study, all extruded ZKL601−*x*Y

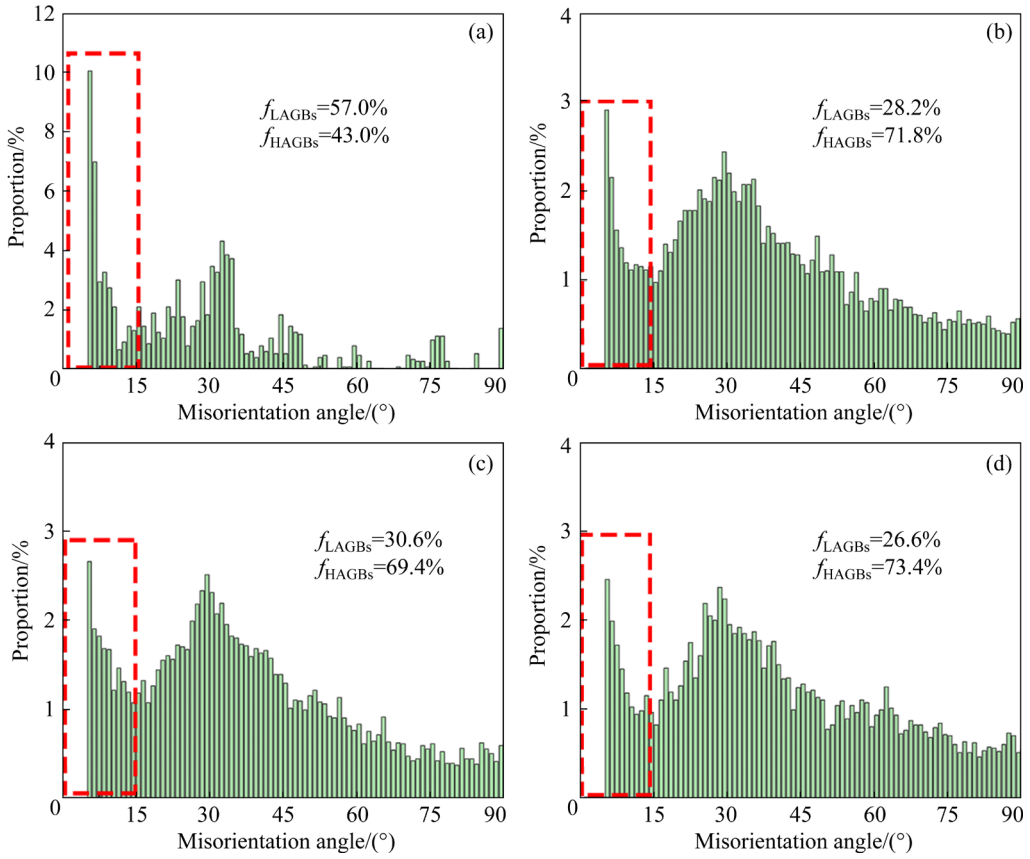

Fig. 15 Misorientation distribution of ZKL601−*x*Y alloys after extrusion: (a) ZKL601; (b) ZKL601−0.5Y; (c) ZKL601−1.0Y; (d) ZKL601−1.5Y

alloys exhibit a bimodal microstructure characterized by the presence of both large and small grains. Extensive research has demonstrated that the coexistence of large and small grains in a bimodal microstructure can contribute to heterogeneous deformation-induced (HDI) strengthening. Therefore, it can be inferred that the strengthening mechanism in the extruded ZKL601−*x*Y alloys comprises grain boundary strengthening, dislocation strengthening, solid solution strengthening, secondary phase strengthening, and HDI strengthening.

Grain boundary strengthening is primarily influenced by the grain size. The Hall−Petch relation demonstrates that the average grain size (d) and YS (σ_{GB}) of the alloy follow the following relationship [26]:

$$\sigma_{GB}=\sigma_0+kd^{-1/2} \quad (1)$$

where σ_0 is the frictional resistance generated when dislocations move in the Mg alloys, and k is the material constant. Grain size and YS exhibit an inverse correlation. The YS of the alloy increases as the average grain size decreases. As shown in Fig. 6, the ZKL601−1.0Y alloy achieves a smaller grain size and higher DRX volume fraction, resulting in the most effective grain boundary strengthening. Furthermore, texture analysis in Figs. 8 and 9 reveals that all ZKL601−*x*Y alloys exhibit a pronounced extrusion texture characteristic (with the *c*-axis parallel to the ED) after the completion of extrusion. The value of the Hall−Petch slope (k) is highly influenced by the grain size and texture, controlling the deformation behavior. Previous studies have demonstrated that a hard orientation of basal slip leads to a larger k value, while a soft orientation results in a smaller k value [26]. The slip system analysis in Fig. 11 indicates lower Schmid factor values for basal slip and a prevalence of hard orientation when loaded along the ED, consequently increasing the k value of the Hall−Petch curve slope. The ZKL601−1.0Y alloy exhibits the strongest basal texture due to the centralized orientation of the DRX grains, thus experiencing the most significant texture hardening effect. Therefore, both grain refinement and texture strengthening contribute to the improved grain

boundary strengthening, with the ZKL601−1.0Y alloy demonstrating exceptional results in terms of grain refinement and texture strengthening.

The significance of the secondary phase in enhancing the mechanical properties should not be overlooked. The extruded ZKL601−*x*Y alloy contains broken micron-sized particle precipitates and dynamically precipitated nanoprecipitates. Dislocations play a crucial role in achieving precipitation strengthening by either shearing or bypassing the precipitates. The dislocation bypassing mechanism is primarily applicable to incoherent precipitates or when the radius of the coherent particles exceeds a critical value. On the other hand, the dislocation shearing mechanism is effective for particles that are resistant to deformation [27]. Within a certain range, there is a positive correlation between the presence of hard-to-deform particles in the alloys and the hindering effect on dislocations. In the extruded ZKL601−*x*Y alloys, broken micron-sized particles and dynamically precipitated nanoprecipitates primarily impede the sliding of dislocations, thereby contributing positively to the strength. The volume fraction of the secondary phase is presented in Fig. 3. It is evident that an increase in the Y content leads to a significant increase in the volume fraction of the secondary phase. As a result, an increase in Y content will greatly enhance the strengthening effect of the secondary phase in the extruded ZKL601−*x*Y alloys.

The influence of La on solid solution strengthening is disregarded due to the limited solid solubility of La in Mg alloys. Zr predominantly exists as monomers in Mg alloys. Therefore, the enhancement effect of solid solution strengthening is solely attributed to Y and Zn. Since the ZKL601−*x*Y alloys have a constant Zn content of 6 wt.%, an increase in Y content results in the formation of Mg−Zn−Y phases, which consumes a portion of the Zn element that is solidly dissolved in the matrix. Consequently, the addition of Y weakens the solid solution strengthening effect of Zn, but introduces solid solution strengthening from Y itself and the secondary phase strengthening of Mg−Zn−Y. These two factors engage in dynamic competition. The following equation is commonly used to assess the solid solution strengthening effect of elements [28]:

$$\sigma_{ss}=\sum(k_i^2 c_i)^{1/2} \quad (2)$$

where c_i is the concentration of solute atoms, k_i is the constant factor related to solute element, and σ_{ss} represents the contribution of solid solution strengthening to YS. The solid solution strengthening effect becomes stronger as the number of solute atoms in the Mg matrix increases. Table 4 shows the content of each element in the matrix of the ZKL601−*x*Y alloys. It is observed that the increase in Y element content in the extruded ZKL601−*x*Y alloys does not result in a noticeable change in the Mg matrix, suggesting that the variation in Y element content does not significantly affect the solid solution strengthening.

Table 4 Contents of solute elements in Mg matrix measured by EDS (wt.%)

Alloy	Zn	Y	La	Zr
ZKL601	1.7	0	0	0.1
ZKL601−0.5Y	1.6	0	0	0.1
ZKL601−1.0Y	1.1	0	0	0.1
ZKL601−1.5Y	1.2	0.1	0.1	0.2

Several studies have demonstrated that the presence of bimodal microstructure can lead to distinct HDI strengthening [29,30]. This phenomenon arises from the disparity in grain sizes between the coarse and fine grains, which leads to the strain incompatibility during the deformation, particularly under room temperature tensile conditions. As a consequence, strain gradients develop at the interfaces between these two types of grains. To accommodate plastic strain, a large number of dislocations quickly accumulate in the coarse grain region, resulting in back stresses and corresponding compressive stresses in the fine grain region. LIU et al [31] have verified that the fine and coarse grain regions of Mg alloys exhibit different strain hardening behaviors during in-situ tensile stretching. The strain incompatibility at the interface of coarse and fine grains causes a transition from a uniaxial stress state to a multiaxial stress state. The DRXed region in the extruded ZKL601−*x*Y alloy is accompanied by a random basal texture, while the deformed region, particularly in areas with larger deformed grains, exhibits a strong basal texture. The presence of a strong basal texture hinders the activation of basal slip in the coarse grains. On the other hand, the random basal texture in the fine grain region

promotes the activation of basal slip. The disparity in texture components between the fine and coarse grain regions amplifies local inhomogeneity and facilitates the transition from basal slip to columnar slip during stretching, thereby increasing HDI stress. Figure 6 presents statistics on the volume fractions of DRXed regions in the extruded alloys. The increase in Y content promotes a slight increase in the DRX volume fraction, but the effect is not significant. Since a higher DRX volume fraction promotes a more uniform stress distribution during the tensile process, the HDI hardening effect is reduced. However, considering that the DRX volume fractions of the alloys in the extruded state do not differ significantly, it can be inferred that the extruded ZKL601−*x*Y alloys do not exhibit a substantial difference in HDI hardening effect.

In conclusion, the YS of the extruded ZKL601−1.0Y alloy is significantly higher than that of the other three alloys. This improvement can be attributed to a combination of grain refinement and textile strengthening, which is further enhanced by grain boundary strengthening. The appropriate Y content facilitates the occurrence of DRX in the alloy, leading to the grain refinement. Additionally, Y element forms a secondary phase at grain boundaries and a small portion of Y solid solution into the Mg matrix, inducing lattice distortion. Both of these effects effectively impede dislocation motion and grain boundary slip, thus enhancing the alloy's strength through fine grain strengthening, solid solution strengthening, and secondary phase strengthening.

4.3 Shielding mechanisms of Y

The increase in Y content significantly enhances the EMI SE of the extruded ZKL601−*x*Y alloys in the low frequency band, while its EMI SE remains largely unaffected in the high frequency band. Previous studies have demonstrated that when electromagnetic waves interact with and pass through a material, three loss mechanisms will occur: reflection loss when the waves contact the material surface, absorption loss within the material due to electromagnetic induction of eddy currents, and multiple reflection loss caused by the impedance mismatch at different interfaces [11]. These three loss mechanisms collectively contribute to the electromagnetic shielding effect of the material.

In general, the reflection loss and absorption loss of electromagnetic waves are closely related to the electrical conductivity. This is primarily because conductivity significantly affects the surface impedance value (Z_s) of the material, that is, higher conductivity results in a higher impedance value. The reflection loss incurred when electromagnetic waves contact the material surface is largely determined by the impedance value of the surface; higher impedance leads to greater reflection loss. Additionally, the electromagnetic induction of eddy currents generated when electromagnetic waves penetrate the material is positively correlated with conductivity [16]. Although the extruded ZKL601−*x*Y alloys exhibit similar conductivities, noticeable differences in EMI SE are observed. Consequently, the contribution of conductivity to the EMI SE of the extruded ZKL601−*x*Y alloys no longer plays a dominant role.

Previous studies have indicated that the EMI SE of Mg alloys is influenced by texture and the presence of secondary phases [32,33]. It is well known that thermal deformation affects the grain orientation of Mg alloys, and extrusion, in particular, results in the development of a strong extrusion texture. Since Mg alloys possess a hexagonal close-packed (HCP) structure, the atomic arrangement along the *a*-axis is considerably denser than that along the *c*-axis. Consequently, the mean free path of free electron motion in the *a*-axis direction is significantly smaller than that in the *c*-axis direction. As a result, the scattering probability of free electrons passing through the *c*-axis is lower compared to that passing through the *a*-axis, leading to higher conductivity along the *c*-axis. Based on this, it can be inferred that the strong basal texture in the extruded ZKL601−*x*Y alloys impacts the impedance between the plate and air, as described by the impedance equation [34]:

$$\sigma=\frac{n_{\mathrm{ef}}e^2l_{\mathrm{F}}}{m^*v_{\mathrm{F}}} \tag{3}$$

where σ is the electrical conductivity, e is the number of electrons, m^* is the effective mass of electrons, v_{F} is the velocity of electron motion, n_{ef} is the number of electrons conducted per unit volume, and l_{F} is the average free range. The statistical analysis of the basal texture in the ZKL601−*x*Y alloys after extrusion reveals that the point of maximum extreme density of the (0001) basal

texture occurs near the TD-axis, and the majority of grains have a perpendicular *c*-axis orientation to the ED−ND plane. The Y content influences the grain orientation in the ZKL601−*x*Y alloys after deformation, with a stronger basal texture resulting in a greater distance between the *c*-axis and the ND of the plate, thereby reducing the impedance difference between the plate and air.

The extruded ZKL601−*x*Y alloys contain various secondary phase structures with different interfacial impedance differences compared to the matrix. When electromagnetic waves penetrate the material, they encounter these interfaces with varying impedance differences, leading to multiple refractions and reflections, which contribute to the multiple reflection loss of electromagnetic waves [35−37]. Additionally, electromagnetic waves enhance the absorption loss due to electromagnetic induction of eddy currents after multiple reflections and refractions. Therefore, the presence of interfaces with different impedance differences in the alloy has a significant impact on electromagnetic wave loss. Statistical analysis of the volume fraction of the secondary phase in the ZKL601−*x*Y alloys after extrusion (Fig. 3) demonstrates that an increase in Y content promotes an increase in the volume fraction of the secondary phase, resulting in higher electromagnetic wave loss. Consequently, the contribution of the secondary phase to the EMI SE of the extruded ZKL601−*x*Y alloys gradually increases with higher Y content. Clearly, an increase in the secondary phase interface is the key factor in achieving high EMI SE in the ZKL601−1.5Y alloy. In the future, regulating the volume fraction of the secondary phase and considering the site-direction relationship could be an effective strategy for achieving high EMI SE.

The analysis results indicate that increasing the Y content significantly improves the EMI SE of the extruded ZKL601−*x*Y alloys. Specifically, a 1 wt.% increase in Y content produces a substantial enhancement in the EMI SE. At room temperature, the UTS, YS, and elongation of the ZKL601−1.0Y alloy are 332.3 MPa, 267.3 MPa, and 16.2%, respectively. Furthermore, the EMI SE in the frequency range of 30−1500 MHz ranges from 79 to 110 dB, making the alloy suitable for various application environments requiring high-toughness electromagnetic shielding materials.

5 Conclusions

(1) Increasing the Y content refines the grain size of the as-cast ZKL601−1.0Y alloys while increasing the proportion of Mg−Zn−RE phases.

(2) The DRX mechanism of the ZKL601−*x*Y alloys during extrusion remains unchanged with increasing Y content. However, an appropriate increase in Y content promotes the DRX behavior.

(3) The ZKL601−1.0Y alloy exhibits a superior balance of strength and plasticity, while the other three Y-content alloys show no significant differences in strength.

(4) The EMI SE of the extruded ZKL601−*x*Y alloys shows a positive correlation with Y content. This is attributed to the increased Mg−Zn−RE phase interfaces resulting from higher Y content.

CRediT authorship contribution statement

Wen-long XU: Software, Data curation, Writing − Review & editing, Writing − Original draft; **Xian-hua CHEN:** Methodology, Supervision; **Lu DENG:** Visualization, Software; **Guan-zheng ZHU:** Visualization, Software; **Yuan YUAN:** Visualization; **Fu-sheng PAN:** Supervision.

Declaration of competing interest

The authors declare that they have no known competing financial interests or personal relationships that could have appeared to influence the work reported in this paper.

Acknowledgments

This research was financially supported from the National Key R&D Program of China (No. 2021YFB3701100), the National Natural Science Foundation of China (No. 52225101), the Fundamental Research Funds for the Central Universities of China (Nos. 2023CDJYXTD-002, 2020CDJDPT001), and the Graduate Research and Innovation Foundation of Chongqing, China (No. CYB23037).

References

[1] KARAKULAK E. A review: Past, present and future of grain refining of magnesium castings [J]. Journal of Magnesium and Alloys, 2019, 7(3): 355−369.

[2] HOU Jun-bin, LI Ding, LIU Ze-jia, JI Zhi-kang, GUAN Shou-fu, LI Chong-chao, QIAO Xiao-guang, GOLOVIN I S, ZHENG Ming-yi. Structure-function integrated magnesium alloys and their composites [J]. Journal of Magnesium and

Alloys, 2023, 11(10): 3511−3544.

[3] NAKATA T, KAMADO S. Towards tailoring basal texture of rolled Mg alloy sheet by recrystallization for high room-temperature formability: A review [J]. Journal of Magnesium and Alloys, 2023, 11(11): 3992−4010.

[4] WU Guo-qin, LI Zhao-can, YU Jian-min, HU Hong-bing, DUAN Ya-li, DONG Bei-bei, ZHANG Zhi-min. Texture evolution and effect on mechanical properties of repetitive upsetting-extruded and heat treatment Mg−Gd−Y−Zn−Zr alloy containing LPSO phases [J]. Journal of Alloys and Compounds, 2023, 938: 168666.

[5] JIN S C, LEE J U, GO J B, YU H, PARK S Y. Effects of Sn addition on the microstructure and mechanical properties of extruded Mg−Bi binary alloy [J]. Journal of Magnesium and Alloys, 2022, 10(3): 850−861.

[6] YE Jun-liu, CHEN Xian-hua, LUO Huan, ZHAO Jie, LI Jian-bo, TAN Jun, YANG Hong, FENG Bo, ZHENG Kai-hong, PAN Fu-sheng. Microstructure, mechanical properties and wear resistance of Ti particles reinforced AZ31 magnesium matrix composites [J]. Journal of Magnesium and Alloys, 2022, 10(8): 2266−2279.

[7] LIU Guan-qi, WANG Kai, PAN Yi-yang, YANG Di, YU Xiao-dong, NIE Zhi-hua, ZHU Jian-hua, HAN Jian-min, TAN Cheng-wen. Effect of Ag content and extrusion on the microstructure and mechanical properties of Mg−Ag alloys [J]. Journal of Materials Research and Technology, 2024, 30: 5916−5926.

[8] LI Yu-xuan, WANG Ming-hui, CAI Jin-long, WANG Chao, DENG Hai, LI Zhi-gang. Effect of Ca addition on microstructure and mechanical properties of Mg−3.8Al−1.1Sn alloys [J]. Materials Today Communications, 2024, 38: 108204.

[9] CHANG Li-li, GUO Jing, SU Xiao-jing. Effect of Y on microstructure evolution and mechanical properties of Mg−4Li−3Al alloys [J]. Transactions of Nonferrous Metals Society of China, 2021, 31(12): 3691−3702.

[10] LEI Bin, WANG Cui-hong, JIANG Bin, BAI Sheng-wen, DONG Zhi-hua, QIAN Xiao-ying, HE Chao, XU Jun-yao, YANG Hua-bao, WANG Qing-hang, PAN Fu-sheng. Role of Y on the microstructure and mechanical properties of Mg−Gd−Zr alloy [J]. Materials Science and Engineering: A, 2022, 861: 144371.

[11] LIU Li-zi, CHEN Xian-hua, PAN Fu-sheng. A review on electromagnetic shielding magnesium alloys [J]. Journal of Magnesium and Alloys, 2021, 9(6): 1906−1921.

[12] XU Wen-long, SU Chang, YUAN Yuan, BAI Jing-ying, CHEN Xian-hua. Achieving excellent electromagnetic interference shielding effectiveness in high rare earth Mg−12Gd−3Y alloy via Nd addition combined with hot rolling and aging [J]. Acta Metallurgica Sinica (English Letters), 2023, 36(10): 1665−1679.

[13] WANG Jia-hao, WU Rui-zhi, FENG Jing, ZHANG Jing-huai, HOU Le-gan, LIU Mei-duo. Recent advances of electromagnetic interference shielding Mg matrix materials and their processing: A review [J]. Transactions of Nonferrous Metals Society of China, 2022, 32(5): 1385−1404.

[14] YE Jun-liu, CHEN Xian-hua, LUO Zhu, LI Jian-bo, YUAN Yuan, TAN Jun, PAN Fu-sheng. Improving strength and electromagnetic shielding effectiveness of Mg−Sn−Zn−Ca−Ce alloy by Sn addition [J]. Advanced Engineering Materials, 2021, 23(9): 2100166.

[15] WANG Jia-hao, SUN Dong-peng, WU Rui-zhi, DU Chun-lin, YANG Zhen-zhao, ZHANG Jing-huai, HOU Le-gan. A good balance between mechanical properties and electromagnetic shielding effectiveness in Mg−9Li−3Al−1Zn alloy [J]. Materials Characterization. 2022, 188: 111888.

[16] LIU Li-zi, CHEN Xian-hua, WANG Jing-feng, QIAO Li-ying, GAO Shang-yu, SONG Kai, ZHAO Chao-yue, LIU Xiao-fang, ZHAO Di, PAN Fu-sheng. Effects of Y and Zn additions on electrical conductivity and electromagnetic shielding effectiveness of Mg−Y−Zn alloys [J]. Journal of Materials Science & Technology, 2019, 35(6): 1074−1080.

[17] XU Wen-long, CHEN Xian-hua, ZHU Guan-zheng, PAN Fu-sheng. Preparation of Mg−6Zn−1Y−0.5Zr alloy sheet with excellent mechanical properties and electromagnetic interference shielding effectiveness by extrusion plus rolling [J]. Materials Characterization, 2024, 207: 113461.

[18] XU Wen-long, CHEN Xian-hua, ZHU Guan-zheng, YUAN Yuan, PAN Fu-sheng. Preparation of Mg−6Zn−1La−0.5Zr alloy sheet with excellent mechanical properties and electromagnetic interference shielding effectiveness by extrusion plus rolling [J]. Journal of Materials Research and Technology, 2023(26): 7740−7756.

[19] ZHENG Tian-xu, HU Yao-bo, JIANG Bin, FU Liang, PAN Fu-sheng, TANG Ai-tao. A comparative study of deformation behaviors and ductility improvement in Mg−Gd−Zr and Mg−Zr cast alloys [J]. Journal of Materials Research and Technology, 2023, 26: 2082−2102.

[20] ZHENG Tian-xu, HU Yao-bo, ZHANG Chao, ZHAO Tian-shuo, JIANG Bin, PAN Fu-sheng, TANG Ai-tao. Uncovering of the formation of rare earth texture and pseudo fiber bimodal microstructure in the high ductility Mg−2Gd−0.4Zr alloy during extrusion [J]. Journal of Materials Science and Technology, 2024, 172: 166−184.

[21] XU Wen-long, CHEN Xian-hua, PAN Fu-sheng, Effect of Y content on the microstructure and mechanical anisotropy of Mg−6Zn−*x*Y−0.5Ce−0.4Zr alloy subjected to asymmetric rolling [J]. Materials Science and Engineering: A, 2023, 882: 145465.

[22] ZHANG Dong-dong, LIU Chu-ming, JIANG Shu-nong, GAO Yong-hao, WAN Ying-chun, CHEN Zhi-yong. Effects of extrusion process on microstructure, precipitates and mechanical properties of Mg−Gd−Y−Zr−Ag alloys [J]. Materials Science and Engineering: A, 2022, 856: 143990.

[23] LI Ming, HUANG Yuan-chun, LIU Yu, WANG Xu, WANG Zhou. Effects of heat treatment before extrusion on dynamic recrystallization behavior, texture and mechanical properties of as-extruded Mg−Gd−Y−Zn−Zr alloy [J]. Materials Science and Engineering: A, 2022, 832: 142479.

[24] XU Wen-long, YU Jian-min, DONG Bei-bei, WANG Qiang, LI Xu-bin, MENG Mu, XU Ping, ZHANG Zhi-min. Deformation temperature impact on microstructure and mechanical properties uniformity of GWZ932K alloy under reciprocating upsetting-extrusion [J]. Journal of Materials Research and Technology, 2022, 16: 1610−1627.

[25] HUANG K, LOGÉ R E. A review of dynamic recrystallization phenomena in metallic materials [J]. Materials and Design, 2016, 111: 548−574.

[26] YU Hui-hui, XIN Yun-chang, WANG Mao-yin, LIU Qing. Hall−Petch relationship in Mg alloys: A review [J]. Journal of Materials Science & Technology, 2018, 34(2): 248−256.
[27] TAHREEN N, ZHANG D F, PAN F S, JIANG X Q, LI D Y, CHEN D L. Strengthening mechanisms in magnesium alloys containing ternary *I*, *W* and LPSO phases [J]. Journal of Materials Science & Technology, 2018, 34(7): 1110−1118.
[28] SUN W T, QIAO X G, ZHENG M Y, XU C, KAMADO S, ZHAO X J, CHEN H W, GAO N, STARINK M J. Altered ageing behaviour of a nanostructured Mg−8.2Gd−3.8Y−1.0Zn−0.4Zr alloy processed by high pressure torsion [J]. Acta Materialia, 2018, 151(1): 260−270.
[29] LIU Shuai-shuai, LIU Han, ZHANG Bao-xuan, HUANG Guang-sheng, CHEN Xiang, TANG Ai-tao, JIANG Bin, PAN Fu-sheng. Effects of extrusion temperature on microstructure evolution and mechanical properties of heterogeneous Mg−Gd alloy laminates via accumulated extrusion bonding [J]. Transactions of Nonferrous Metals Society of China, 2022, 32(7): 2190−2204.
[30] LIU Shuai-shuai, ZHANG Bao-xuan, HUANG Guang-sheng, ZOU Qin, TANG Ai-tao, JIANG Bin, PAN Fu-sheng. Achieving strength−ductility synergy of AZ91 extruded sheet by balancing dual-heterostructure of grain size and precipitates [J]. Materials Science and Engineering: A, 2021, 827: 141989.
[31] LIU Shuai-shuai, XIA Da-biao, YANG Hong, HUANG Guang-sheng, YANG Fei-xiang, CHEN Xian-hua, TANG Ai-tao, JIANG Bin, PAN Fu-sheng. Mechanical properties and deformation mechanism in Mg−Gd alloy laminate with dual-heterostructure grain size and texture [J]. International Journal of Plasticity, 2022, 157: 103371.
[32] LUO Zhu, CHEN Xian-hua, SONG Kai, LIU Chun-quan, DAI Yan, ZHAO Di, PAN Fu-sheng. Effect of alloying element on electromagnetic interference shielding effectiveness of binary magnesium alloys [J]. Acta Metallurgica Sinica (English Letters), 2019, 32(7): 817−824.
[33] SONG K, PAN F S, CHEN X H, ZHANG Z H, TANG A T, SHE J, YU Z W, PAN H C, XU X Y. Effect of texture on the electromagnetic shielding property of magnesium alloy [J]. Materials Letters, 2015, 157(0): 73−76.
[34] GALL D. Electron mean free path in elemental metals [J]. Journal of Applied Physics, 2016, 119(8): 085101.
[35] GAO Shang-yu, CHEN Xian-hua, PAN Fu-sheng, SONG Kai, ZHAO Chao-yue, LIU Li-zi, LIU Xiao-fang, ZHAO Di. Effect of secondary phase on the electromagnetic shielding effectiveness of magnesium alloy [J]. Scientific Reports. 2018, 8(1): 1625.
[36] WANG Jia-hao, JIN Si-yuan, WU Rui-zhi, XU Lin, ZHANG Jing-huai, FENG Jing, HOU Le-gan, JIAO Yun-lei. Improvement of electromagnetic shielding properties for Mg−8Li−6Y−2Zn alloy by heat treatment and hot rolling [J]. Journal of Materials Science: Materials in Electronics, 2020, 31(20): 17249−17257.
[37] WANG Jia-hao, DU Chun-lin, WU Rui-zhi, XU Lin, FENG Jing, ZHANG Jing-huai, Hou Le-gan, LIU Mei-duo, LIU Bin. Effect of Li content on electromagnetic shielding effectiveness in binary Mg−Li alloys: A combined experimental and first-principles study [J]. Journal of Materials Science: Materials in Electronics, 2022, 33(7): 3891−3900.

Y 含量对 Mg−6Zn−*x*Y−1La−0.5Zr 合金力学性能和电磁屏蔽效能的影响

徐文龙[1,2]，陈先华[1,2]，邓 璐[1,2]，朱官政[3]，袁 媛[1,2]，潘复生[1,2]

1. 重庆大学 材料科学与工程学院，重庆 400045；
2. 重庆大学 国家镁合金材料工程研究中心，重庆 400045；
3. 中国航发贵阳发动机设计研究所，贵阳 550014

摘 要：研究了 Y 含量对 Mg−6Zn−*x*Y−1La−0.5Zr 合金显微组织、力学性能和电磁屏蔽效能的影响。经挤压处理后，Mg−6Zn−*x*Y−1La−0.5Zr 合金未发生动态再结晶的粗大晶粒沿着挤压方向被拉长，小尺寸的再结晶晶粒分布于大晶粒四周。Mg−6Zn−1Y−1La−0.5Zr 合金表现出较为优异的强度和塑性的平衡，其极限抗拉强度、屈服强度和伸长率分别为 332.3 MPa、267.3 MPa 和 16.2%。同时在 30~1500 MHz 的频率范围内电磁屏蔽效能为 79~110 dB，符合大多数高强电磁屏蔽材料的应用需求环境。

关键词：Mg−Zn−Y−La−Zr 合金；动态再结晶；显微组织；力学性能；电磁屏蔽效能

(Edited by Wei-ping CHEN)